# Fabrication, modelling and use of porous ceramics for ultrasonic transducer applications

F. Levassort · J. Holc · E. Ringgaard · T. Bove · M. Kosec · M. Lethiecq

**Abstract** Porous ceramics are of interest for ultrasonic transducer applications. Porosity allows to decrease acoustical impedance, thus improving transfer of acoustical energy to water or biological tissues. For underwater applications, the $d_h g_h$ figure of merit can also be improved as compared to dense materials. In the case of high frequency transducers, namely for high resolution medical imaging, thick film technology can be used. The active films are generally porous and this porosity must be controlled. An unpoled porous PZT substrate is also shown to be an interesting solution since it can be used in a screen-printing process and as a backing for the transducer. This paper describes the fabrication process to obtain such materials, presents microstructure analysis as well as functional properties of materials. Modelling is also performed and results are compared to measurements. Finally, transducer issues are addressed through modelling and design of several configurations. The key parameters are identified and their effect on transducer performance is discussed. A comparison with dense materials is performed and results are discussed to highlight in which cases porous piezoceramics can improve transducer performance, and improvements are quantified.

F. Levassort (✉) · M. Lethiecq
Laboratoire Ultrasons Signaux Instrumentation,
Francois-Rabelais University,
LUSSI, 10 boulevard Tonnellé, BP 3223,
Tours cedex 1 37032, France
e-mail: levassort@univ-tours.fr

J. Holc · M. Kosec
Jozef Stefan Institute, Jamova 39,
Ljubljana 1000, Slovenia

E. Ringgaard · T. Bove
Ferroperm Piezoceramics A/S, Hejreskovvej 18A,
Kvistgaard 3490, Denmark

## 1 Introduction

The combination of two materials having different properties (such as elastic or dielectric) allows to deliver several advantages that one of the materials cannot offer alone. This principle has been applied with a piezoelectric phase and an inert phase at the end of the 1970s. The spatial distribution between the two phases is of great importance since it is the main point which determines the effective properties of the piezocomposite. For this, the concept of connectivity has been defined to classify the different possibilities [1, 2]. Many studies and publications have been performed to optimise the choice of the connectivity and the properties of each phase. Recently, a description of fabricated piezoelectric composites has been given in a review article for actuators and sensors [3]. Among all these possibilities, this paper is focused on porous piezoelectric ceramics which can be considered as a biphasic ceramic-air (or polymer) composite and the highlighted applications concern ultrasonic transducers. In this context, a large variety of processing techniques have been used to deliver porous ceramics with large ranges of pore volumes, pore size distributions, pore shapes, and also thickness of the sample [4].

Two main applications are studied here. The first is the development of an integrated structure including several porous ceramic materials for high frequency medical imaging. For this, porous piezoelectric thick film is fabricated with a screen-printed process. The thick film is deposited on an unpoled porous PZT substrate. For transducer applications, such a substrate has several advantages and can be used as a backing. The first is the

high temperature stability during the sintering of the piezoelectric thick film. Also, the similar composition of the two elements limits the chemical diffusion and avoids a decrease of the piezoelectric performance of the thick film. The porosity allows to control the acoustical impedance in the substrate and to increase the attenuation, allowing to minimise the thickness to assume for which it can be considered as a semi-infinite medium.

The second application is the development of bulk porous ceramics for medical, industrial and underwater applications. For these applications, modelling is performed, namely homogenisation of the porous ceramics and then prediction of transducer properties to evaluate the improvement brought by porous ceramics in comparison with standard dense ceramics.

The next section briefly describes the different fabrication processes used for the applications described above (i.e. porous unpoled PZT substrate, piezoelectric thick film and bulk porous PZT ceramics). Section 3 first reports the characterisation of functional properties of piezoelectric elements in thickness mode. The specific behaviour of bulk porous ceramics has particularly been investigated as a function of frequency. Secondly, the modelling of a porous ceramic is described. The model is based on a generalisation of series and parallel connections to deduce the effective electro-elastic moduli of the material. The model results are compared to several experimental values of bulk porous ceramic. This model is also exploited to simulate the behaviour of the hydrostatic strain coefficient ($d_h$) and corresponding figure of merit ($d_h \times g_h$). In Section 4, properties of simulated transducers based on bulk porous ceramics are first calculated and compared to those using dense ceramics. The improvement of transducer properties are then quantified in terms of sensitivity and bandwidth. Finally, the description and discussion of the use of an integrated structure for high frequency applications are presented. The importance of the control of the volume fraction of porosity between the different layers is highlighted and it is shown how the properties of the corresponding high frequency transducers can be optimised.

# 2 Fabrication process and microstructure characterisation

Porous ceramics can be produced by adding pore formers with different contents and size. The pore former burns out during sintering process forming cavities which increase the porosity of sintered material. Pore fraction, size and distribution of pore size as well as morphology are controlled by the amount of added pore former. Pore formers are mainly organic or fugitive inorganic compounds which decompose and/or burn out at relatively low temperature such as starch [5], PVA [6], graphite [7], β-dextrin [8]. This method is used for the substrate fabrication.

## 2.1 Substrate

$Pb(Zr_{0.53}Ti_{047})O_3$-PZT powder was prepared by mixed-oxide synthesis at 900 °C for 2 h using PbO (Aldrich, 99.9%), $ZrO_2$ (Tosoh, 99%) and $TiO_2$ (Fluka, 99%) as starting materials. Synthesised powder was ball milled in zirconia planetary mill in acetone for 2 h. A fine particle size powder of a mean particle size of 1.88 μm as measured by granulometry (Cilas) was obtained.

Pore formers were added into PZT to obtain the porous structure. Three different chemicals were used as pore formers, polyethylene glycol-PEG (molar mass 4,000), saccharose (common sugar) and ammonium oxalate (Riedel-de Haen). Powder mixtures with 15 and 20 vol.% of pore former were prepared by homogenisation in zirconia ball mill in acetone. After drying, the powders were pressed in a steel die into the test pellets with a pressure of 100 MPa. Pellets were presintered at 600 °C with heating rate of 1 K/min and sintered at 1,200 °C for 2 h with heating rate of 5 K/min in $PbZrO_3$ packing powder. Samples were also tested by applying subsequent sintering at 1,200 °C for 2 h. This procedure simulates the firing processes of electrode and thick film material during thick film structure preparation. Samples were characterised by microstructural and stereological analysis. The average pore size was determined from thermally etched cross sections. In the first step of analysis, the pores from each image were redrawn on a transparent foil. The redrawn images of grains were then scanned. Such digitised images were further analysed by an image processing software. The surface of each pore was measured and its size was calculated as a diameter for circular geometry. Geometrical density of pellets was calculated from dimensions and mass. Relative density (RD) defined as percentage of theoretical value for pore-free PZT ($8,000$ kg/m$^3$) was then calculated from geometrical density.

Substrates for fabrication of transducers were prepared by pressing PZT powder with addition of 15 vol.% of ammonium oxalate with pressure of 100 MPa into pellets with 8 mm diameter and 14 mm height. Pellets were sintered at same sintering conditions as test samples. After the sintering process, the substrates were lapped in to final dimensions: diameter 5 mm and height 10 mm.

Relative density of samples with addition of 15 and 20 vol.% of ammonium oxalate, PEG and saccharose after sintering at 1,200 °C for 2 h are shown in Fig. 1. For comparison, the density of PZT sintered at same conditions is added. With addition of 15 vol.% of pore formers, the relative density drops from 97% TD for pure PZT to around 88% TD for ammonium oxalate, 93% TD for PEG and 90% TD for saccharose, respectively. With addition of 20 vol.%
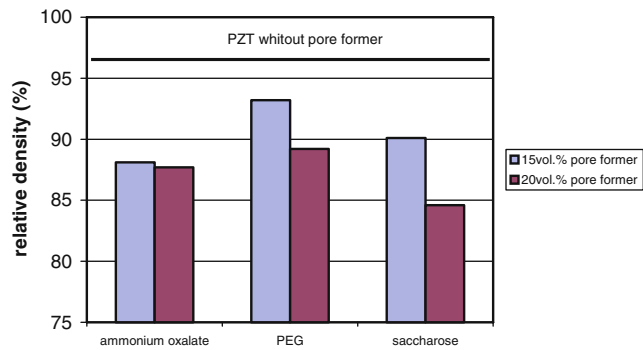
**Fig. 1** Relative density of PZT samples with addition of 15 and 20 vol.% of pore former after sintering at 1,200 °C for 2 h

of pore formers to PZT the density sees a further decrease of 3% for PEG, 5% for saccharose, but remains nearly the same as for addition of 15 vol.% for ammonium oxalate. The microstructures of polished and thermally etched samples of PZT with addition of 15 vol.% of pore formers are shown in Fig. 2. In the samples with addition of ammonium oxalate and saccharose, the pores are equally distributed over the cross section. In the sample with addition of PEG, both small pores are visible on the etched sample and very large pores up to 100 μm visible on polished cross section sample. The mean pore size for all samples measured from the etched samples are given in Table 1. The presence of small and large pores in the sample with addition of PEG is evident and due to the non-uniform pore size distribution obtained, PEG is not an optimum pore former. The pore size for samples with addition of ammonium oxalate and saccharose are similar and are comparable to grain size (Fig. 2).

However, contrary to saccharose, ammonium oxalate decomposes into gas products e.g. water, ammonia and carbon dioxide without any solid residuals. From the

**Fig. 2** Microstructure of the PZT samples with addition of 15 vol.% of pore formers after sintering at 1,200 °C for 2 h (First row-ammonium oxalate, second row-PEG and third row-saccharose)
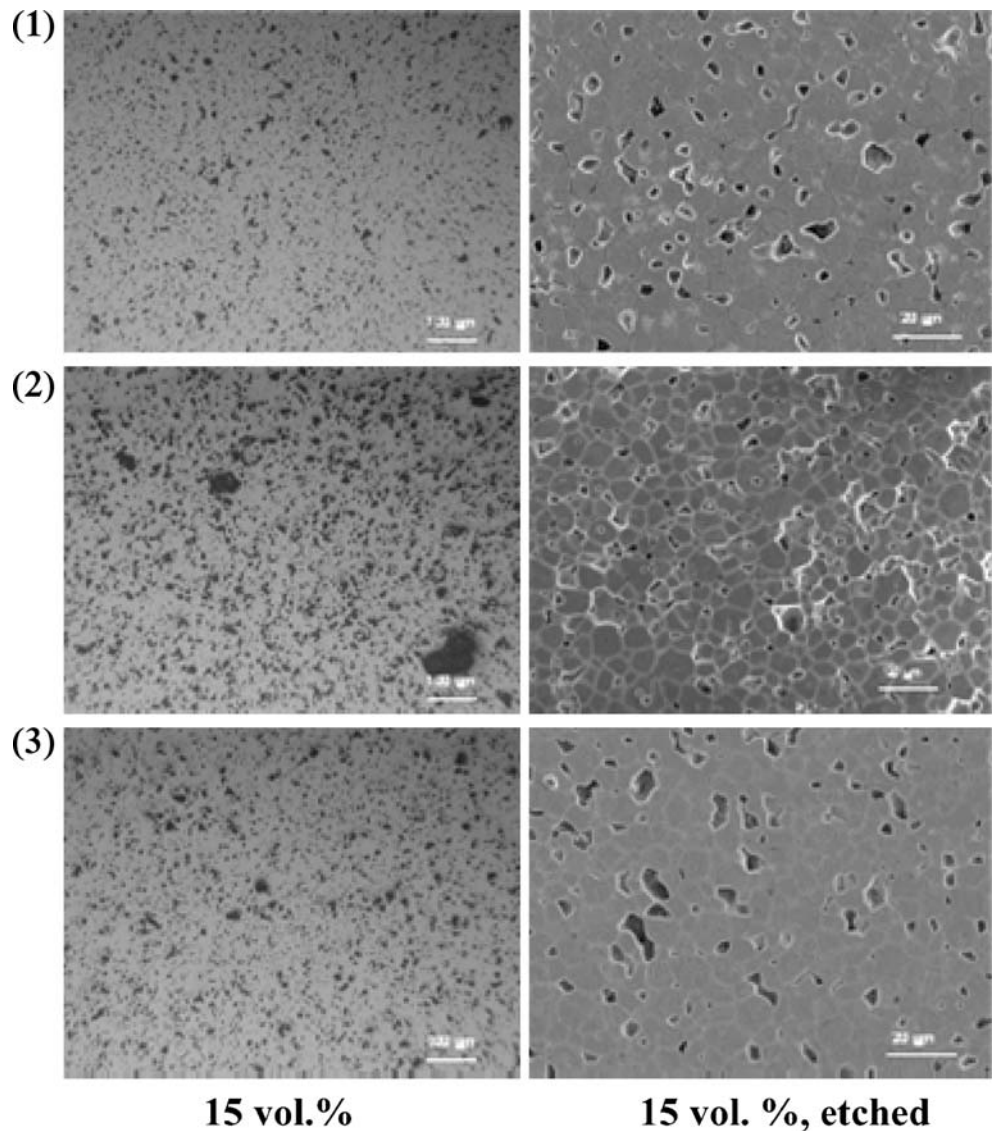
**Table 1** Mean pore diameter for PZT samples with addition of 15 vol. % pore formers after sintering at 1,200 °C for 2 h.

| Pore former (15 vol.%) | Mean pore diameter ($\mu$m) |
|---|---|
| Ammonium oxalate | 4.0 |
| PEG | 2.7 |
| Saccharose | 4.1 |

obtained results, ammonium oxalate was chosen as material to make porous substrate for transducer.

Samples with ammonium oxalate addition were also tested by subsequent sintering at 1,200 °C for 2 h. The results are shown in Table 2. This procedure simulates the firing processes of electrode and thick film material during thick film structure preparation. The results show that the porous PZT produced by addition of ammonium oxalate pore former is stable as the density remains practically the same after subsequent sintering procedure.

## 2.2 Thick films

PZT 53/47 powder (PbZr$_{0.53}$Ti$_{0.47}$O$_3$) with an excess of 6 mol% of PbO was prepared by mixed-oxide synthesis at 900 °C for 1 h from high-purity PbO, ZrO$_2$, and TiO$_2$. To this was added 2 wt.% of lead germanate, with the composition Pb$_5$Ge$_3$O$_{11}$ as a sintering aid. Lead germanate (PGO) was also prepared by mixed-oxide synthesis from PbO and GeO$_2$ (Ventron, 99%) at 700 °C. After synthesis, both compositions were ball milled in acetone for 1 h and dried.

Thick film ink was prepared from the mixed PZT and PGO powder (PZT/PGO) and an organic vehicle ($\alpha$-terpineol, butyl carbitol, and ethyl cellulose) by mixing them in a roll-mill. Viscosity of the paste was optimized by changing mass ratio of powder and organic vehicle. Pastes with viscosity around 20 Pa.s were used for printing.

The thick-film structure was prepared by first printing two barrier layers of PZT/PGO with intermediate drying at 150 °C on the porous PZT substrate described in the previous paragraph. This structure was over-printed with gold thick film conductor (Ferro, type 3,261) and was fired at 800 °C for 8 h. Over this, PZT active films were printed six times with intermediate drying. Samples were sintered in closed alumina container at 800 °C for 8 h. Dense PZT thick film was

**Table 2** Relative density of PZT samples with addition of 15 vol.% of ammonium oxalate after sintering at 1,200 °C for 2 h and subsequent sintering at same temperature for 2 h.

| Ammonium oxalate (vol%) | 1,200 °C, 2 h relative density (%) | 1,200 °C, 2+2 h relative density (%) |
|---|---|---|
| 15 | 88.1 | 88.6 |
| 20 | 87.7 | 88.8 |

obtained with firing of samples at the same temperature in closed alumina container with small amount PbZrO$_3$ to provide lead oxide rich atmosphere. Upper gold electrode was produced by magnetron sputtering at room temperature through metallic mask. PZT/PGO film was polarised with electric field of 10–12 kV/mm at 160 °C in oil bath.

## 2.3 Bulk ceramics

Ferroperm Piezoceramics A/S have three commercial types of piezoceramics based on porous PZT, namely a standard soft-doped composition (Pz37), a hard-doped composition (Pz36) and a high-permittivity composition (Pz39). Table 3 gives an overview of key properties. These ceramics are manufactured using a specialised process allowing to introduce highly controlled porosity both in terms of volume fraction and size by means of an organic pore former. The relative porosity has been optimised by adjusting the amount of pore former in order to obtain desired acoustic properties (for example, in Table 3, the volume fraction of porosity in Pz37 is 20%).

## 3 Functional characterisation and modelling

### 3.1 Characterisation

For the experimental functional characterisation, a HP4395A network analyser and corresponding impedance test-kit were used to measure electrical impedance as a function of frequency of the porous piezoelectric element. An electrical equivalent circuit model (KLM) [9, 10] was used to fit the electrical impedance and allowed the thickness mode characteristics in free mechanical resonator conditions to be deduced.

First, two batches of bulk ceramics composed of porous PZT (Pz37) and dense soft-PZT have been characterised. The dense soft-PZT ceramic corresponds to the matrix of the porous PZT ceramic. Seven samples of Pz37 have been characterised and their corresponding antiresonance frequencies are between 1.1 to 8.4 MHz. Their silver electrodes have a thickness of around 5 $\mu$m. Their effects on the electrical impedance spectra are not negligible. These electrodes are taken into account in the KLM model to deduce the properties of the piezoelectric material. The volume fraction of porosity for these samples ($v_p$=25± 1.5%) is slightly higher than those presented in Table 3. Eight samples of dense soft-PZT that have comparable resonance frequencies are also characterised for comparison.

In order to increase the frequency range of the study and deduce the behaviour of several parameters as a function of frequency, the overtones of the thickness mode are also fitted up to 36 MHz. Thickness coupling factors and

**Table 3** Selected properties of three commercial porous piezoceramic materials from Ferroperm Piezoceramics A/S, all based on PZT.

| Material | | Pz36 | Pz37 | Pz39 |
|---|---|---|---|---|
| $\rho$ | (kg/m$^3$) | 5.7 | 6.5 | 5.8 |
| $Z_a$ | (MRa) | 14 | 19 | 14 |
| $\varepsilon_{33,r}$ | | 610 | 1,200 | 1,750 |
| tan $\delta$ | | 0.003 | 0.017 | 0.019 |
| $T_C$ | (°C) | 350 | 350 | 220 |
| $k_p$ | (%) | 26 | 38 | 18 |
| $k_t$ | (%) | 52 | 52 | 53 |
| $d_{33}$ | (pC/N) | 230 | 380 | 480 |
| $N_t$ | (Hz m) | 1,270 | 1,470 | 1,190 |

$\rho$: density; $Z$: acoustic impedance; $\varepsilon_{33,r}$: Relative permittivity; tan $\delta$: dielectric loss tangent; $T_c$: Curie temperature; $k_p$: planar coupling factor; $k_t$: thickness coupling factor; $d_{33}$: piezoelectric charge coefficient; $N_t$: thickness frequency constant.

mechanical losses results are shown in Fig. 3. Points corresponding to porous PZT are in black while those corresponding to dense soft-PZT are in gray. Linear regressions analysis has been performed on the parameters (thickness coupling factor and mechanical losses) to quantify the frequency dependence. Significant differences are observed. For the mechanical losses, a value of $-1.5$ $10^{-3}$ MHz$^{-1}$ for dense soft-PZT is measured while for the porous PZT, the corresponding value is an order of magnitude higher ($-19.6$ $10^{-3}$ MHz$^{-1}$). The porosity is mainly responsible for this increase of mechanical losses. Moreover, an analysis of the microstructure and in particular the grain size distribution shows that the mean grain size is two times higher in the dense soft-PZT than in the porous PZT ceramic [11]. This result contributes to differentiate the behaviour of the mechanical losses. This high frequency dependence observed for the porous ceramic leads to a limited frequency range (up to around 8.5 MHz) since the high order overtones are not observed. A variation of the thickness coupling factor is also measured. In Table 4, the thickness mode characteristics (fundamental) of four representative samples (two dense soft-PZT and two porous PZT) are summarised. For the fundamental mode, the corresponding value is slightly higher for porous PZT than for dense PZT, but the frequency dependence is different (Fig. 3). The consequence is that under 8 MHz, the tendency is reversed as also noticed in Table 4.

For the screen-printed thick film, which has been deposited on a gold plated substrate, the determination of thickness mode parameters is more difficult than for a free resonator. In this case, the thick film can be considered as one of the constitutive layers of a multilayer structure. Several authors have calculated the electrical impedance for several layers [12]. Here, an electrical KLM circuit is again used to simulate the electrical impedance of the structure (between the two electrodes of the thick film) composed of

five layers (porous unpoled PZT substrate, porous barrier layer, bottom electrode, screen-printed thick film and front electrode). Knowing the thickness of each layer and their acoustical properties (except the thick film), the electromechanical properties of this thick film can be deduced [13, 14]. Two examples of properties of PZT/PGO thick film obtained by the fabrication process described in Section 2.2 are summarised in Table 5. These properties will be discussed in terms of high frequency transducer applications in Section 4.

### 3.2 Modelling

To calculate the effective parameters of composites with different connectivities, many approaches and theories have been investigated. Several theories have been extended to piezoelectric materials [15, 16] and applied to piezocomposites such as Eshelby's theory (inclusion and inhomogeneity problems) [17–19] and in particular to porous piezoelectric ceramics [20]. Other authors have used different effective medium theories to calculate effective electro-elastic moduli of piezocomposites including porous piezoelectric ceramics (3–0 or 3–1 connectivity) [21–25]. Finite element method has also been used to study the properties of 3–3 connectivity materials [26]. The modelling used in this paper is based on a method developed in
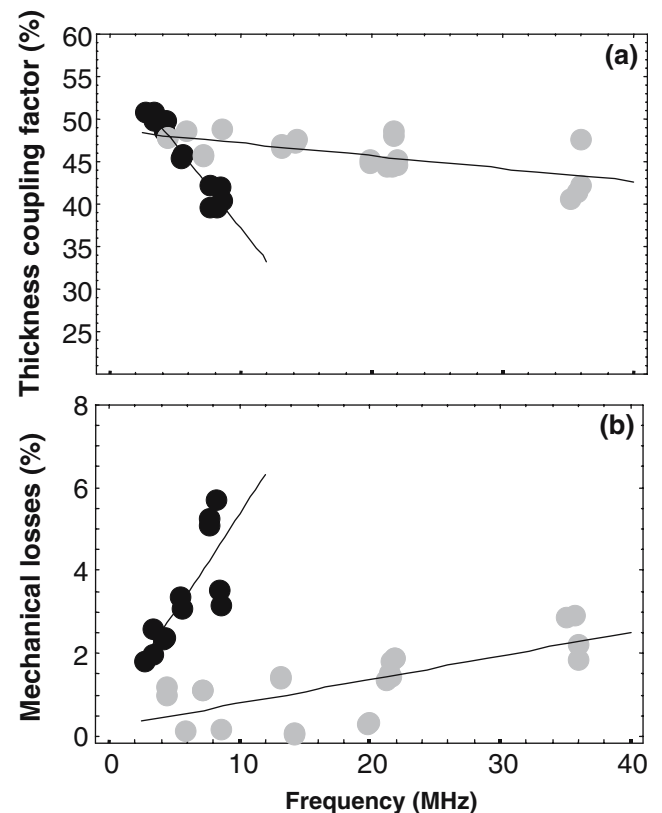


**Fig. 3** (a) Thickness coupling factor ($k_t$) and (b) mechanical losses ($\delta_m$) as a function of frequency for dense soft PZT (*gray points*) and Pz37 (*black points*)

**Table 4** Characteristics of four dense soft-PZT and porous Pz37 samples.

| | $t$ ($\mu$m) | $\rho$ (kg/m$^3$) | $f_a$ (MHz) | $v_l$ (m/s) | $Z$ (MRa) | $k_t$ (%) | $\varepsilon_{33}^S/\varepsilon_0$ | $\delta_m$ (%) |
|---|---|---|---|---|---|---|---|---|
| 1-Soft-PZT | 505 | 7,680 | 4.3 | 4,410 | 33.9 | 47.9 | 790 | 1.0 |
| 2-Pz37(porous) | 328 | 5,680 | 4.2 | 2,775 | 15.7 | 49.8 | 550 | 2.4 |
| 3-Soft-PZT | 315 | 7,750 | 7.2 | 4,540 | 35.4 | 45.8 | 850 | 1.1 |
| 4-Pz37 (Porous) | 173 | 5,710 | 8.4 | 2,910 | 16.6 | 42.1 | 600 | 3.5 |

$t$: thickness; $\rho$: density, $f_a$: antiresonant frequency; $v_l$: longitudinal wave velocity; $Z$: acoustical impedance; $k_t$: thickness coupling factor; $\varepsilon_{33}^S/\varepsilon_0$: dielectric constant at constant strain; $\delta_m$: mechanical losses.

previous work, and adapted to porous piezoelectric materials [27–29]. Here, the method is based on the generalisation of series and parallel connections (corresponding to 2–2 connectivity) [30] and modified cubes model [31].

In a porous ceramic, the spatial arrangement between the pores and the dense phase can be defined according to the fabrication process and the volume fraction of porosity in the material. Two possible connectivities can be formed (i.e. 3–0 and 3–3) and can be present jointly in the material as shown on the schematic representation in Fig. 4. Several of the models recalled at the beginning of this paragraph are limited in the number of possible connectivities since the inhomogeneity shape is often considered as ellipsoidal (3–0 connectivity). For this shape, extreme cases can be obtained when one or two of the axes of the ellipsoidal inhomogeneity tend towards infinity (which corresponds to 3–1 and 2–2 connectivities). The 3–3 connectivity cannot be obtained with these models, even if for high volume fractions, interaction between inhomogeneities can be taken into account.

The representative unit cubic cell used in this paper contains the two phases where the inhomogeneity shape (i.e. pore shape) is directly related to the connectivity (Fig. 5). In this way, large varieties of connectivities are possible and in particular the 3–3 connectivity [32–34]. For the 3–0 connectivity [35], the cubic shape inhomogeneity in a corner is isolated (closed porosity) and characterised by the dimension parameter b. For 3–3 connectivity, the inhomogeneity is assumed to be in contact in the three directions corresponding to an open porosity, and is placed in the opposite corner. This inhomogeneity is represented with three branches where each length is unit and a is the characteristic parameter (Fig. 5). The total porosity volume fraction $v_p$ is obtained using the two independent variables a and b to calculate the volume of the two inhomogeneities

knowing that the volume of the cell is unit. Moreover, a proportion of 3–0 connectivity, noted p, can be defined in the whole cell. This proportion is expressed as a ratio between the porosity volume fraction in 3–0 connectivity to the total porosity volume fraction in the cell:

$$p = \frac{b^3}{3a^2 - 2a^3 + b^3} \qquad (1)$$

Finally, the total porosity volume fraction can be expressed as a function of p and a by eliminating the variable b:

$$v_p = 3a^2 - 2a^3 + \frac{p(2a^3 - 3a^2)}{(p-1)} \qquad (2)$$

For the calculation of effective properties, only the principle is recalled here, detailed description can be found in [29]. The basis of this matrix method is to define two vectors ($G$) and ($H$) which each contain nine components. These components are obtained with 18 boundary conditions on the stress and strain tensors as well as electrical field and electrical displacement vectors. The vector ($G$) gathers all the nine constant parameters through the two phases material while ($H$) contains the nine other spatially averaged quantities. For these definitions, the two phase material must be in 2–2 (series or parallel) or 1–3 connectivities. These two vectors depend only on the position of the interfacial layers along the third axis (Fig. 5, i.e. poling direction), consequently they describe the connectivity of the two-phase material. To homogenise the unit cell of Fig. 5 and deduce the effective electro-elastic moduli of the considered material, it must be decomposed into six blocks (where each constitutive block is in 2–2 connectivity). Each block is first homogenised separately and then the cell is re-

**Table 5** Characteristics of two screen-printed piezoelectric thick films on porous PZT substrate.

| Piezoelectric material | $R$ (mm) | $t$ ($\mu$m) | $v_l$ (m/s) | $f_a$ (MHz) | $f_0$ (MHz) | $\varepsilon_{33}^S/\varepsilon_0$ | $k_t$ (%) | $\delta_e$ (%) | $\delta_m$ (%) | $Z$ (MRa) |
|---|---|---|---|---|---|---|---|---|---|---|
| (a) PZT/PGO | 1.06 | 43 | 3,300 | 38.3 | 24.0 | 370 | 48.5 | 0.05 | 9.8 | 17.9 |
| (b) PZT/PGO | 2.02 | 32 | 4,300 | 67 | 42 | 510 | 41 | 0.5 | 20 | 29.8 |

$R$: radius of the upper electrode; $t$: thickness; $v_l$: longitudinal wave velocity; $f_a$: antiresonant frequency; $\varepsilon_{33}^S/\varepsilon_0$: dielectric constant at constant strain; $k_t$: thickness coupling factor; $\delta_e$: dielectric losses; $\delta_m$: mechanical losses; $Z$: acoustical impedance.
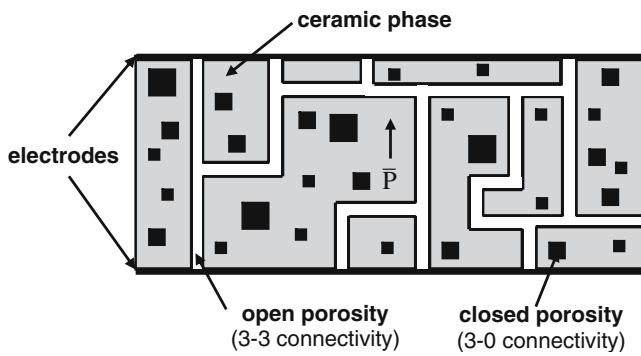
**Fig. 4** Schematic representation of porous piezoelectric ceramic containing both 3–0 (*with black porosity*) and 3–3 connectivities (*with white porosity*)

assembled successively in 2–2 or 1–3 connectivities. At each of these steps, the corresponding volume fraction is re-calculated. With this method, as we can easily notice in the unit cell (Fig. 5), a compactness limit is reached before a complete unit fraction of porosity (if $b=1-a$). Therefore, an alternative solution can be used which consists in a description of "composite of composite." First, the dense ceramic phase can be homogenised considering only the isolated inhomogeneity (3–0). Then a 3–3 composite can be defined where the matrix is now the homogenised 3–0 composite as schematically described in Fig. 6. The second step is to homogenise a "standard" 3–3 composite [28]. The corresponding connectivity of such a material can be noted 3–3(3–0). The porosity

volume fraction in 3–0 connectivity, noted p, can varied between 0 to 1 to calculate the two pure connectivities ($p=0$ for 3–3 connectivity and 1 for 3–0 connectivity).

The main advantage of this simple matrix method is that all the effective components of the elastic, dielectric and piezoelectric tensors are simultaneously obtained as a function of the porosity volume fraction. All this data allows parameters such as the coupling factors to be easily calculated. Moreover, the transversely isotropic symmetry of the dense ceramic is kept for the effective electro-elastic moduli.

Material data used for simulations is that of the dense soft-PZT (the matrix), given in Table 6. In this material, a porosity volume fraction around 2–3% is generally observed, but it is neglected here. Thus, a small error is induced in the calculation. For the porosity phase, air characteristics are used.

The acoustical impedance (Fig. 7) is deduced from the effective elastic constant $c_{33}^D$ and the density $\rho$ as a function of the porosity volume fraction. The mean value of all experimental results on Pz37 samples in paragraph 3.1 is also added (black point). This result confirms that the experimental acoustical impedance is between those of the
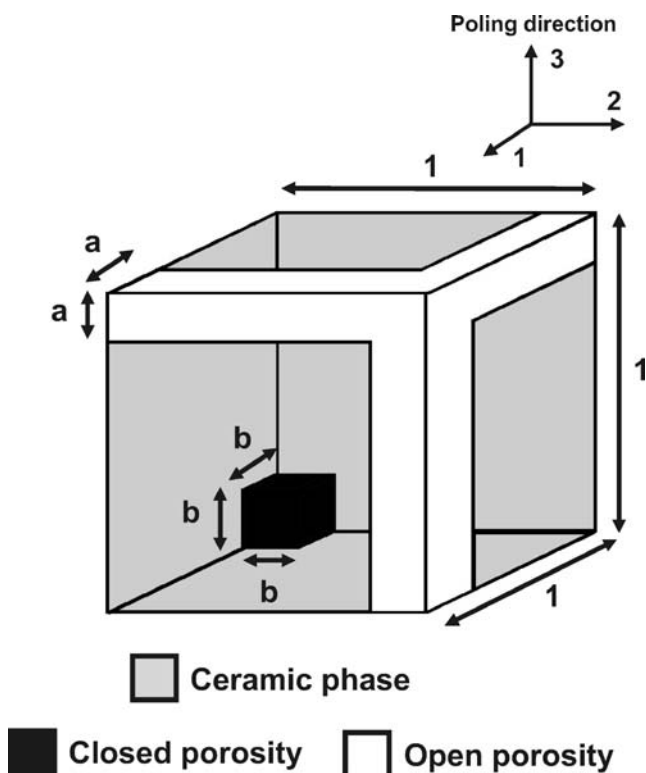


**Fig. 5** Definition of the unit cell for 3–3 and 3–0 connectivities representing a porous piezoelectric ceramic, with the coordinate system
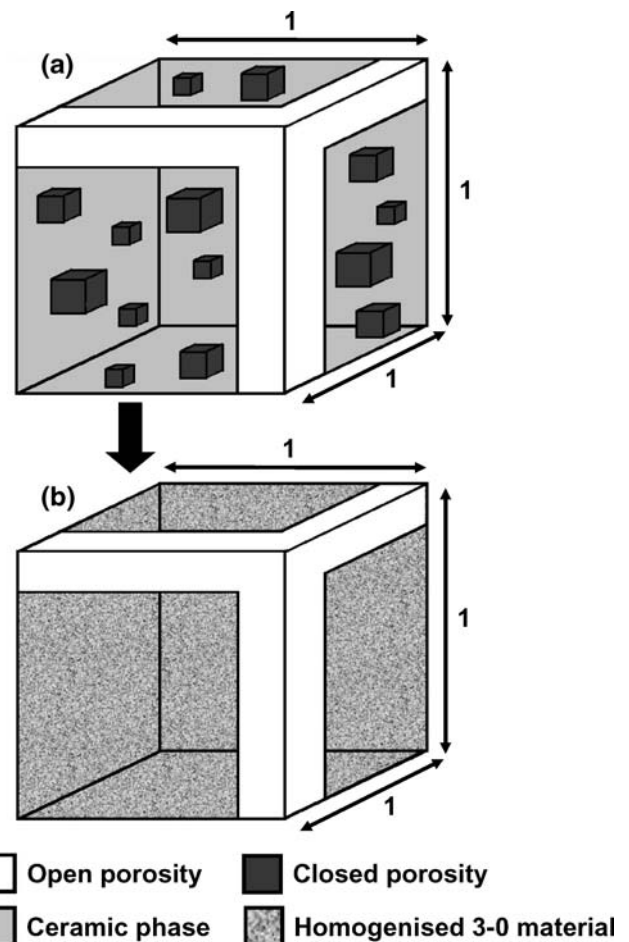


**Fig. 6** (a) Unit cell of the representation of the composite of composite 3–3(3–0). (b) 3–3 connectivity unit cell where the homogenized 3–0 composite is considered as the matrix

**Table 6** Elastic, piezoelectric and dielectric characteristics of dense-soft PZT.

| $C_{11}^E$ $(10^{10}$ N/m$^2$) | $C_{12}^E$ $(10^{10}$ N/m$^2$) | $C_{13}^E$ $(10^{10}$ N/m$^2$) | $C_{33}^E$ $(10^{10}$ N/m$^2$) | $C_{44}^E$ $(10^{10}$ N/m$^2$) | $e_{33}$ (C/m$^2$) | $e_{13}$ (C/m$^2$) | $e_{15}$ (C/m$^2$) | $\varepsilon_{11}^S/\varepsilon_0$ | $\varepsilon_{33}^S/\varepsilon_0$ | $\rho$ (kg/m3) |
|---|---|---|---|---|---|---|---|---|---|---|
| 14.28 | 9.98 | 9.22 | 11.45 | 2.28 | 15.77 | −3.71 | 11.74 | 1,121 | 878 | 7,750 |

two pure 3–0 (black solid line) and 3–3 connectivities (grey solid line). For the dielectric constant (Fig. 8), experimental results are close to those of pure 3–0 connectivity (variations are shown through a vertical bar).

This model can also be used to simulate other parameters for transducer applications. Optimisation of the thickness coupling factor is required to deliver transducers with high performance. Figure 9 shows the behaviour of this parameter as a function of the porosity volume fraction for the two connectivities (3–3 in gray and 3–0 in black). The fictive constitutive materials of the pores have a Young's modulus of 5 and 1 GPa, as mentioned on each curve. The other pore phase parameters such as Poisson ratio, relative dielectric constant and density have been kept constant and the corresponding values are, respectively, 0.37, 3.9 and 1,170 kg/m$^3$. Results show that for the two connectivities, the thickness coupling factor can be higher that of dense PZT ceramic. For 3–3 connectivity, highest values are delivered for relatively low volume fractions of porosity (here between 20 and 40%) while for 3–0 connectivity, the maximum is found above 40%. The properties of the materials used as the pores also have an influence on the effective parameters. The values of the thickness coupling factor increase if Young's modulus decreases. This result is consistent if the pore phase is considered as air. The shape of the pores also has an influence on the effective parameters. Our model assumes that porosity shape is cubic for 3–0 and that the lengths of the three branches for 3–3 connectivities are equal. Several authors have shown that if the lengths of each of the three branches are different for 3–3 connectivity, large differences

can be obtained on effective parameters. If the vertical branch (in the poling direction) is privileged, effective piezoelectric coefficients and thickness coupling factor can be increased [26, 36]. This observation is due to the fact that 1–3 connectivity (with the vertical branch) becomes predominant which significantly increase the performance while the two horizontal branches (in series for the homogenisation) contribute mainly to increase the porosity volume fraction but not, for example, the piezoelectric activity. This has also been studied in the case of reticulated ceramics [37, 38].

Another important application is underwater acoustics for which hydrostatic properties of the porous piezoelectric material are the key parameters [39–42]. An active transducer sensitivity can be characterised by the hydrostatic strain coefficient $d_h$ defined by :

$$d_{\mathrm{h}} = \mathrm{d}_{33} + 2\mathrm{d}_{31}\left(\mathrm{C.N}^{-1}\right) \qquad (3)$$

The performance of a hydrophone (passive transducer) can be evaluated with the hydrostatic piezoelectric voltage coefficient ($g_h$) defined by:

$$g_{\mathrm{h}} = \frac{d_{\mathrm{h}}}{\varepsilon_{33}^T} \qquad (4)$$

For a transducer alternatively used in transmit and receive modes, the figure of merit ($d_h g_h$) can be used. Figures 10 and 11 give, respectively, the hydrostatic strain coefficient ($d_h$) and the figure of merit ($d_h g_h$) using the same data set for simulations as for Fig. 9. Again, the decrease of the Young's modulus of the pore phase allows to increase the effective parameters and the maximum
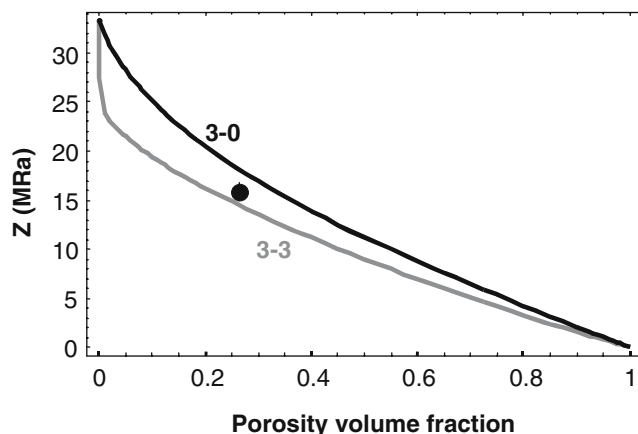


**Fig. 7** Acoustical impedance as a function of the porosity volume fraction for 3–0 and 3–3 connectivities
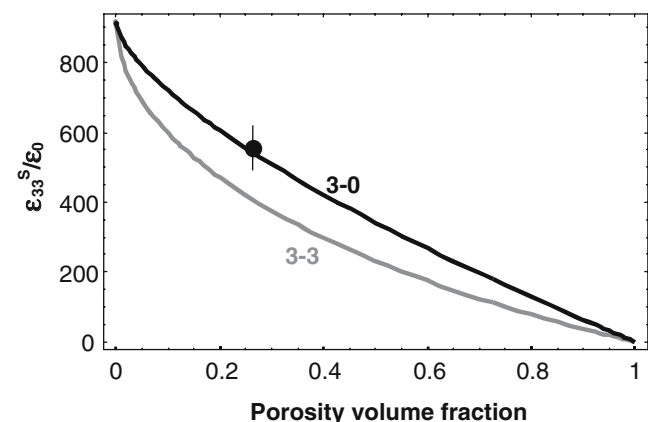


**Fig. 8** Relative dielectric constant $\varepsilon_{33}^S/\varepsilon_0$ as a function of the porosity volume fraction for 3–0 and 3–3 connectivities
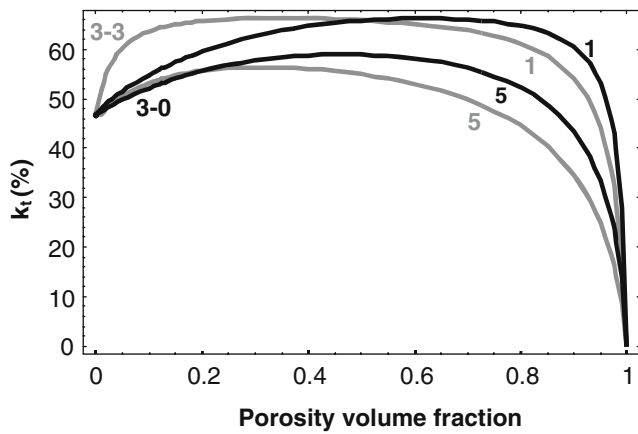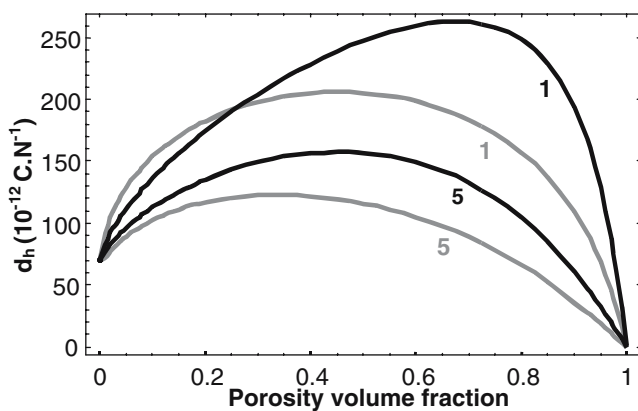
**Fig. 9** Thickness coupling factor $k_t$ as a function of the porosity volume fraction for 3–0 (*solid black lines*) and 3–3 (*solid gray lines*) connectivities. Two sets of curves are calculated for Young's modulus of 5 and 1 GPa

values are always shifted towards a higher porosity volume fraction [34, 43]. These results show that the configurations chosen here, the 3–0 connectivity delivers higher performance than the 3–3 connectivity. Specific studies have also been performed on the effect of complex connectivities [44] or data used (such as the ratio $-d_{33}/d_{31}$ of the matrix ceramic) to optimise several effective parameters [45, 46].

# 4 Applications to transducers

## 4.1 Performance comparisons

Several simulations have been performed with the KLM model to evaluate and compare the performance of different configurations of simple transducers based on dense soft-PZT or porous PZT (data of Pz37). For this, data from Table 4 with sample 1 (dense PZT) and 2 (porous PZT) have been used. All the simulation results are summarised



**Fig. 10** Hydrostatic strain coefficient $d_h$ as a function of the porosity volume fraction for 3–0 (*solid black lines*) and 3–3 (*solid gray lines*) connectivities. Two sets of curves are calculated for Young's modulus of 5 and 1 GPa
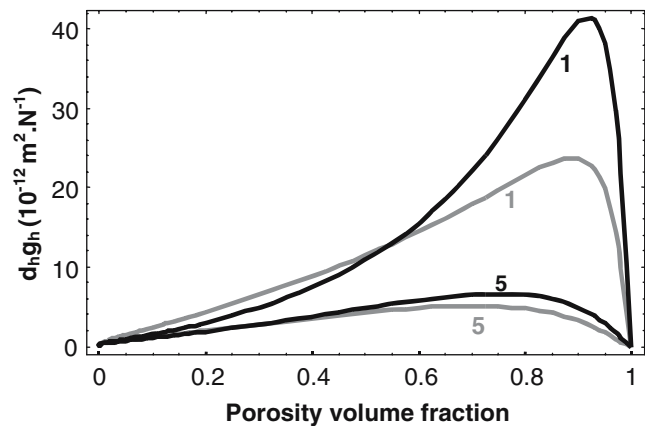


**Fig. 11** Hydrostatic figure of merit $d_h\, g_h$ as a function of the porosity volume fraction for 3–0 (*solid black lines*) and 3–3 (*solid gray lines*) connectivities. Two sets of curves are calculated for Young's modulus of 5 and 1 GPa

in Table 7. For these piezoelectric elements, a change in data from Table 4 has been made concerning the thickness coupling factor value. Indeed, in order to only take into account the influence of the porosity (through the acoustical impedance value), the ($k_t$) value of the dense soft-PZT (47.9%) is also used for the Pz37 data. Moreover, electrical conditions are fixed with a generator input impedance of $Z_g$=0 Ω and a receiver with $Z_r$=1 MΩ. These conditions allow to avoid taking into account the area of the electrodes and electrical environment. All the simulations used water as propagation medium and the backing is considered as a semi-infinite medium. The centre frequency of all the corresponding transducers is at 3.9 MHz.

The two first simulated transducer configurations are composed only of a backing and the piezoelectric elements (dense soft-PZT and Pz37). A backing with an acoustical impedance of 9.5 MRa is chosen to deliver a relative bandwidth at −6 dB of 30% for the transducer integrating the dense soft PZT element. For an easier comparison, the acoustical impedance of the backing has been adjusted for the transducer based on Pz37 to keep the same bandwidth. In this case, comparison between the two simulations can be directly observed on the sensitivity, calculated in dB. Results show an increase of sensitivity of 6 dB with the porous PZT ceramic. Electroacoustic responses are shown in Fig. 12.

If a matching layer is added, the sensitivity is logically increased for both materials, but the difference is lower than in the previous set of simulations (0.5 dB) (Fig. 12). This small improvement is associated with a significant increase of bandwidth at −20 dB (10%). The characteristics of the matching layer (thickness typically around a quarter wavelength and acoustical impedance) have been optimised with a performance index. This performance index is composed of three characteristics of the electroacoustic response of the transducer. The characteristics are related to the duration at −6 and −30 dB and the amplitude of the pulse-echo response.

**Table 7** Characteristics and performance of three simulated transducers.

| | Transducer characteristics | | | Transducer performance | | |
|---|---|---|---|---|---|---|
| | $Z_b$ (MRa) | $Z_{m1}$ (MRa) | $Z_{m2}$ (MRa) | IL (dB) | BW (−6 dB) (%) | BW (−20 dB) (%) |
| Pz27 | 9.5 | – | – | −14.9 | 30 | 86 |
| Pz37 | 3.6 | – | – | −8.8 | 30 | 86 |
| Pz27 | 9.5 | 4.3 | – | −4.2 | 43 | 81 |
| Pz37 | 3.6 | 2.6 | – | −3.7 | 43 | 91 |
| Pz27 | 9.5 | 6.7 | 2.4 | −3 | 58 | 98 |
| Pz37 | 2.2 | 4.6 | 2.0 | 0 | 58 | 103 |

$Z_b$: acoustical impedance of the backing; $Z_{m1}$: acoustical impedance of the first matching layer; $Z_{m2}$: acoustical impedance of the second matching layer; $IL$: insertion loss (normalised with the last configuration); $BW(−6dB)$: Relative bandwidth at −6 dB; $BW(−20$ dB): Relative bandwidth at −20 dB.

These three parameters are weighted for medical applications through an adequate trade-off found between bandwidth and sensitivity of the transducer [47].

Finally, with two matching layers and a fixed bandwidth at −6 dB of 58% the sensitivity is 3 dB higher with Pz37 (Fig. 12). All the calculated sensitivities have been normalised with this last configuration (considered at 0 dB). In these three sets of simulations (0, 1 and 2 matching layers), the Pz37 porous piezoceramic allows to increase the performance of transducers, in particular when no matching layer is used. If the measured value of $k_t$ is used for the Pz37 sample (i.e. 49.8%), the sensitivity is further increased by 1 dB with a configuration using two matching layers.
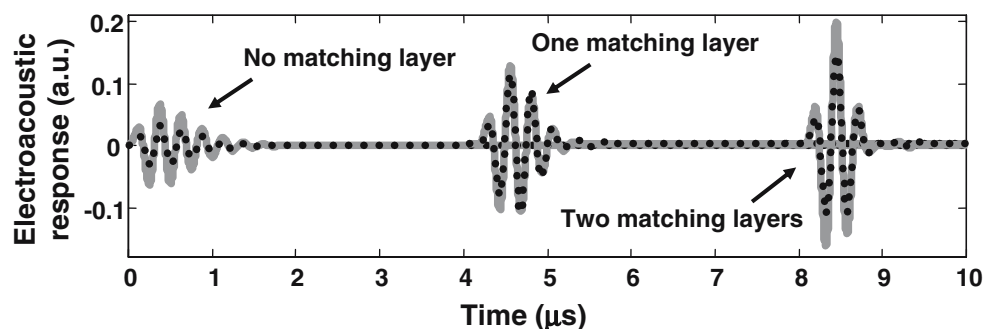
4.2 High frequency transducer applications

The structures described in Section 2 of passive porous PZT substrate and PZT/PGO thick film are used to fabricate high frequency transducers. The electromechanical properties of two thick films have been recalled in Table 5. Photographs of one of the samples obtained and a cross section observed by SEM of the integrated structure with the thick film (b) in Table 5 are, respectively, shown on Figs. 13 and 14. The layers contain different volume fractions of porosity and the corresponding values have a significant influence on the final properties of high frequency transducers integrating these structures.

The volume fraction of porosity in the substrate has been measured (14%, see paragraph 2.1) and an evaluation of the acoustical properties can be made (including longitudinal wave velocity) using the matrix method described in paragraph 3.2. This can be performed assuming that all the piezoelectric coefficients are null for this unpoled ceramic. As observed on Fig. 2, the connectivity of the microstructure can be considered as 3–0 (closed porosity). The effective longitudinal wave velocity and the acoustical impedance as a function of volume fraction of porosity are calculated (Fig. 15). For our case ($v_p$=14%), they are, respectively, 2,730 m/s and 18.2 MRa. These parameters have been used as fixed data to evaluate the properties of piezoelectric thick film [14] as explained in paragraph 3.1.

The importance of the difference of porosity contents between the piezoelectric thick film and the substrate are clearly shown in Fig. 16. On this figure are represented the complex electrical impedance spectra of the two thick films in the multilayer structures. For the first one (a) the thick film corresponds to reference (a) from Table 5. In this configuration, the volume fraction of porosity in the thick film (around 30%) is higher than in the porous PZT substrate. This result has been obtained on several samples of a same batch where the porosity has been determined by stereological analysis of the polished microstructures through measurement of the pore areas using image analysis. This observation implies that the resonant frequency of the thick



**Fig. 12** Comparisons of electroacoustic responses of simulated transducers (*black dotted responses*: with porous PZT ceramic, *gray solid responses*: with dense soft-PZT) for three configurations (no matching layer, with one matching layer, with two matching layers)

**Fig. 13** Photographs of the multilayer structure fabricated for high frequency transducer application
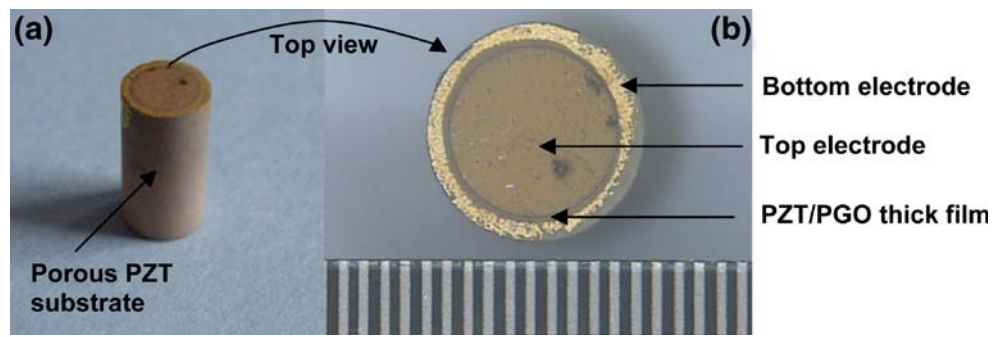


film is dramatically decreased in comparison of a resonator (of same thickness) in free mechanical conditions. Here, the antiresonant frequency is around 25 MHz. This has been improved by slightly modifying the fabrication process of the screen-printed piezoelectric thick film to deliver a denser material than the previous case. As shown in Fig. 14, the porosity of the new thick film is lower than in the substrate (properties of this film are in Table 4, case b). Figure 16(b) shows that the antiresonant frequency is now over 40 MHz. Even if the second thick film has a lower thickness, this change does not explain all the increase of resonant frequency. The ratio of the porosity between the two constitutive elements is a key parameter to control this resonant frequency. The thickness of the bottom electrode which has a high acoustical impedance in comparison with the two other porous elements also has an influence on the acoustic behaviour of the structure (the electrode is around 5 μm thick in both cases). Obtaining a higher resonance frequency for the transducer integrating such structures allows to improve the axial resolution [48].

Finally, to compare the performance of the integrated structure in a high frequency transducer (piezoelectric thick film properties (a) of Table 5 have been used with the porous PZT substrate and a gold bottom electrode of 7 μm) with that of a standard configuration using a light backing (acoustical impedance of 5 MRa), impulse pressure waveforms transmitted into water have been calculated in the two cases using the KLM model. An optimised matching

layer has been added in both cases. Results show a 3 dB higher sensitivity for the standard configuration, but its relative bandwidth at −6 dB is lower (i.e. 51% compared to 70% for the porous PZT substrate transducer).

## 5 Conclusion

Different studies have been performed related to the development and use of porous ceramics for ultrasonic transducer applications. A fabrication process of bulk porous PZT ceramics was briefly described and batches of these materials have been characterised as a function of frequency to deduce their corresponding behaviour, in particular the thickness coupling factor and mechanical losses. Results showed that frequency dependence of these parameters are significantly higher than those measured on dense PZT ceramics corresponding to the matrix of the porous material. Transducer simulations have also permitted to quantify an increase of sensitivity at constant bandwidth for those integrating porous PZT ceramic in comparison with those based on standard dense soft-PZT. A simple configuration of a single element transducer with a backing, a porous PZT (Pz37) disc and no matching layer in water allows a 6 dB increase in sensitivity to be obtained.
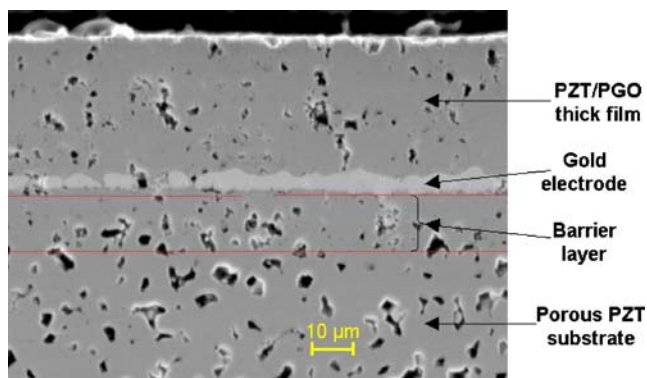


**Fig. 14** SEM cross section of the structure developed for high frequency transducers
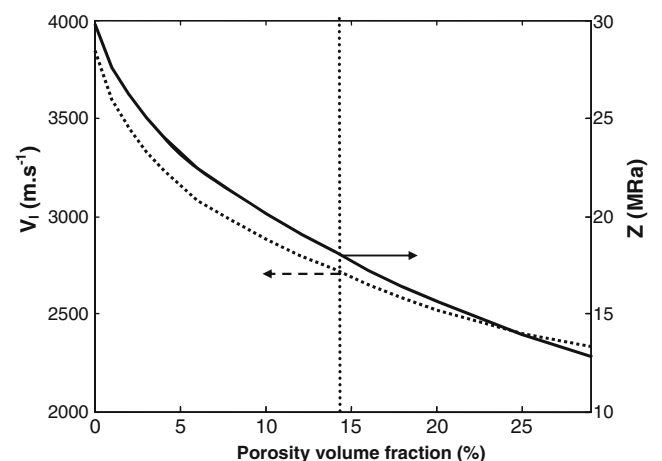


**Fig. 15** Homogenised longitudinal wave velocity (*dashed line*) and acoustic impedance (*solid line*) of unpoled PZT ceramic according to volume fraction of porosity

**Fig. 16** Real and imaginary parts of the electrical impedances of two PZT/PGO-based multilayer structure measured between the two piezoelectric thick film electrodes as a function of frequency (*black solid lines* : modelling, *gray dotted lines* : experimental values). (**a**) and (**b**) correspond respectively to samples a and b from Table 4
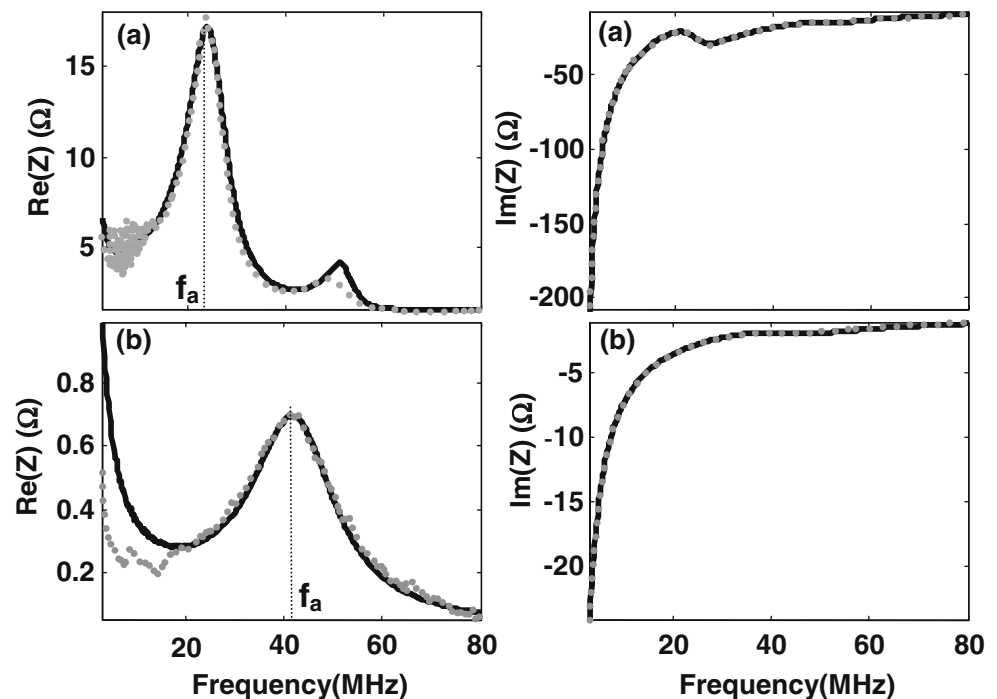
Fabrication process of an integrated structure for high frequency ultrasonic transducers has been described. For this, an unpoled PZT porous backing with 14% porosity volume fraction is made and used to deposit by screen-printing PZT/PGO thick films having high electromechanical performance (the thickness coupling factor is over 40%). This structure can be directly used to fabricate a single element transducer for high frequency medical imaging [14]. The critical point in the fabrication process is the control of the porosity in the different layers. In particular, to maximise the resonance frequency of the structure, it is desirable to have a higher volume fraction of porosity in the substrate than in the piezoelectric thick film. This observation is valid if the bottom electrode and barrier layer are sufficiently thin to minimise their contributions on the acoustical resonance of the structure.

Finally, modelling of piezoelectric porous ceramics has been performed. The porous ceramic is represented by a unit cubic cell including inhomogeneities which allow to calculate electro-elastic moduli of 3–0 and 3–3 connectivities corresponding to extreme cases of the behaviour of a composite of composite with 3–3(3–0) complex connectivity. Results have been compared to experimental data of porous PZT ceramic (Pz37). The values of acoustical impedance and relative dielectric constant are between those of the pure 3–0 and 3–3 connectivities calculated with the model. These observations are consistent with the microstructure, in particular the relatively high volume fraction of porosity (25%). The model was also successfully applied to calculate hydrostatic parameters for underwater hydrophones and the figure of merit for emitter-receiver transducers. Effective parameters obtained are comparable to those calculated by several other authors. As shown through the different applications addressed in this study, porous ceramics can be used to increase the performance of ultrasonic transducers.

## References

1. R.E. Newnham, D.P. Skinner, L.E. Cross, Mater. Res. Bull. **13**, 525–536 (1978)
2. D.P. Skinner, R.E. Newnham, L.E. Cross, Mater. Res. Bull. **13**, 599–607 (1978)
3. E.K. Akdogan, M. Allahverdi, A. Safari, IEEE Trans. Ultrason. Ferroelect. Freq. Contr. **52**(5), 746–775 (2005)
4. C. Galassi, J. Eur. Ceram. Soc. **24**(14), 2951–2958 (2006)
5. O. Lyckfeldt, J.M.F. Ferreira, Eur. Ceram. Soc. **184**, 134–140 (1998)
6. W.J. Chao, K.S. Chou, Key Eng. Mater. **113**, 96–108 (1996)
7. D. Piazza, C. Capiani, C. Galassi, J. Eur. Ceram. Soc. **25**, 3075–3078 (2005)
8. T. Zeng, X.L. Dong, S.T. Chen, H. Yang, Ceram. Int. **33**(3), 395–399 (2006)
9. R. Krimholtz, D.A. Leedom, G.L. Matthei, Electronic Letters **38**, 338–339 (1970)
10. S. Van Kervel, J.M. Thijssen, Ultrasonics **21**, 134–140 (1983)
11. M. Lethiecq, F. Levassort, L.P. Tran Huu-Hue, M. Alguero, L. Pardo, T. Bove, E. Ringgaard, W. Wolny, *New low acoustic impedance piezoelectric material for broadband transducer applications*. IEEE Ultrasonics Symposium Proceedings 1153–1156 (2004)
12. M. Lukacs, T. Olding, M. Sayer, R. Tasker, S. Sherrit, J. Appl. Phys. **85**(5), 2835–2843 (1999)

13. F. Levassort, L.P. Tran-Huu-Hue, J. Holc, T. Bove, M. Kosec, M. Lethiecq, *High performance piezoceramic films on substrates for high frequency imaging*. IEEE Ultrasonics Symposium Proceedings 1035–1038 (2001)
14. P. Maréchal, F. Levassort, J. Holc, L.P. Tran-Huu-Hue, M. Kosec, M. Lethiecq, IEEE Trans. Ultrason. Ferroelect. Freq. Contr. **53**(8), 1524–1533 (2006)
15. W.F. Deeg, *The Analysis of Dislocation, Crack, and Inclusion Problems in Piezoelectric Solids*. Ph.D. Thesis, Stanford University (1980)
16. M.L. Dunn, Int. J. Eng. Sci. **32**(1), 119–131 (1994)
17. J.D. Eshelby, *The determination of the elastic field of an ellipsoidal inclusion, and related problems*. Proc. R. Soc. Lond. 376–396 (1957)
18. M.L. Dunn, M. Taya, *An analysis of piezoelectric composite materials containing ellipsoidal inhomogeneities*. Proc. R. Soc. Lond. 265–287 (1993)
19. M.L. Dunn, M. Taya, Int. J. Solids Struct. **30**(2), 161–175 (1993)
20. M.L. Dunn, M. Taya, J. Am. Ceram. Soc. **76**, 1697–1706 (1993)
21. C.W. Nan, F.S. Jin, Phys. Rev., B **48**(12), 8578–8582 (1993)
22. C.W. Nan, J. Appl. Phys. **76**(2), 1155–1163 (1994)
23. B. Wang, Int. J. Solids Struct. **29**(3), 293–308 (1992)
24. B. Wang, S. Du, Int. J. Appl. Electromagn. Mater. **3**, 289–295 (1993)
25. T.E. Gomez Alvarez-Arenas, F. Montero de Espinosa, J. Acoust. Soc. Am. **102**(6), 3507–3515 (1997)
26. A. Perry, C.R. Bowen, Scripta Materiala **41**(9),1001–1007 (1999)
27. F. Levassort, M. Lethiecq, D. Certon, F. Patat, IEEE Trans. Ultrason. Ferroelect. Freq. Contr. **44**(2), 445–452 (1997)
28. F. Levassort, M. Lethiecq, C.E. Millar, L. Pourcelot, IEEE Trans. Ultrason. Ferroelect. Freq. Contr. **45**(6), 1497–1505 (1998)
29. F. Levassort, M. Lethiecq, R. Desmare, L.P. Tran-Huu-Hue, IEEE Trans. Ultrason. Ferroelect. Freq. Contr. **46**(4), 1028–1034 (1999)
30. K.Y. Hashimoto, M. Yamaguchi, *Elastic, Piezoelectric and Dielectric Properties of Composite Materials*. IEEE Ultrasonics Symposium Proceedings 697–702 (1986)
31. H. Banno, Ferroelectrics **50**, 3–12 (1983)
32. K. Rittenmeyer, T. Shrout, W.A. Schulze, R.E. Newnham, Ferroelectrics **41**, 189–195 (1982)
33. H. Banno, Jpn. J. Appl. Phys. **32**, 4214–4217 (1993)
34. C.R. Bowen, A. Perry, H. Kara, S.W. Mahon, J. Eur. Ceram. Soc. **21**, 1463–1467 (2001)
35. S.M. Pilgrim, R.E. Newnham, Mater. Res. Bull. **21**, 1447–1454 (1986)
36. C.R. Bowen, H. Kara, Mater. Chem. Phys. **75**, 45–49 (2002)
37. M.J. Creedom, W.A. Schulze, Ferroelectrics **153**, 333–339 (1994)
38. M.J. Creedom, W.A. Schulze, *Large area piezoelectric composite arrays from distorted reticulated ceramics*. IEEE Ultrasonics Symposium Proceedings 527–530 (1996)
39. R.Y. Ting, Ferroelectrics **67**, 143–157 (1986)
40. T. Arai, K. Ayusawa, H. Sato, T. Miyata, K. Kawamura, K. Kobayashi, Jpn. J. Appl. Phys. **30**, 2253–2255 (1991)
41. P. Guillaussier, C.A.D. Boucher, Ferroelectrics **187**, 121–128 (1996)
42. S. Marselli, V. Pavia, C. Galassi, E. Roncari, F. Craciun, G. Guidarelli, J. Acoust. Soc. Am. **106**(2), 733–738 (1999)
43. H. Kara, R. Ramesh, R. Stevens, C.R. Bowen, IEEE Trans. Ultrason. Ferroelect. Freq. Contr. **50**(3), 289–296 (2003)
44. V.Yu. Topolov, A.V. Turik, Tech. Phys. **46**(9), 1093–1100 (2001)
45. V.Yu. Topolov, A.V. Turik, Tech. Phys. Lett. **27**(1), 81–83 (2001)
46. C.R. Bowen, V.Yu. Topolov, Acta Mater. **51**, 4965–4976 (2003)
47. R. Desmare, L.P. Tran-Huu-Hue, F. Levassort, M. Lethiecq, Journal Revista de Acustica **33** (2003)
48. F.S. Foster, C.J. Pavlin, K.A. Harasiewicz, D.A. Christopher, D.H. Turnbull, Ultrasound Med. Biol. **26**(1), 1–27 (2000)